Supporting Information

Xie et al. 10.1073/pnas.1218569110

I. SI Materials and Methods

I.1. Marine Sediment Samples. Microbially active surface sediments were sampled in February 2010 from the upper tidal flat of the German Wadden Sea near Wremen (53° 38′ 0N, 8° 29′ 30E). The sediment was oxidized at the surface and anoxic below about 2 cm, with a dark color suggesting high levels of reduced compounds. Subtidal and intertidal sediments from the Wadden Sea region of the North Sea are readily mixed and frequently exposed to oxic and anoxic conditions (1). Frequent inputs of fresh organic matter may cause rapid shifts in the prevailing microbial conditions. These surface Wadden Sea sediments harbor a large diversity of microbial communities—archaeal and bacterial, sulfate reducing and methanogenic (2, 3). Deep subsurface sediments were recovered from northern Cascadia Margin during Integrated Ocean Drilling Program Expedition 311 [site U1326, 138.2 meters below seafloor (mbsf), in situ temperature 20 °C, water depth 1,828 m (4)]. Site U1326 is located on an uplifted ridge of accreted sediments (4). The sample used in this study is situated in the methanogenic zone (4), and its location coincides with the maximum of alkalinity that is a typical feature of deep methanogenic zones (5). The sulfate–methane transition zone was placed at 2.5 mbsf; methane concentrations were high below this depth. Low sulfate levels scattering around 3 mM in deeper intervals may have been caused by contamination with seawater during drilling (4). Until preparation of sediment slurries, both sediment types were stored at +4 °C in 0.5-L Schott bottles without headspace, sealed with a black rubber stopper.

I.2. Preparation of Sediment Slurries. Before the slurries were prepared, samples were stored at atmospheric pressure for 6 mo (Wadden Sea) and 4 y (Cascadia Margin); all experiments were conducted under atmospheric pressure. Anoxic sediment slurries were prepared in a glove box [Coy Laboratory Products Inc.; atmosphere: 3% (vol/vol) H_2 in N_2] by mixing 0.5 L sediment with approximately the same volume of sterilized, sulfate-free artificial seawater (in grams·L^{-1} of deionized water: KCl, 0.68; $CaCl_2{\cdot}2H_2O$, 1.5; $MgCl_2{\cdot}6H_2O$, 11.3; NaCl, 26.4; KBr, 0.10; $NaHCO_3$, 0.84). Sediment slurries were stored in a series of 1-L Schott bottles with ∼500 mL headspace, which was exchanged with pure N_2 (1 bar). Sterilized slurries (by threefold heating for 25 min to 120 °C) were produced as a control for nonbiological degradation of the intact polar lipids (IPLs). Afterward, water was removed and replaced by freshly autoclaved artificial seawater. Estuarine surface sediment contained substantial levels of sulfate. To deplete sulfate, we preincubated the slurries at room temperature in the dark. After 1 mo, a subsample was taken out and filtered through a 0.45-μM filter for sulfate measurement. Sulfate was measured in 1:50 diluted samples via suppressed ion chromatography with conductivity detection on a 761 Compact IC (Metrohm AG) equipped with a Metrosep A Supp 5–100 column with a carbonate eluent (3.2 mmol·L^{-1} Na_2CO_3/1 mmol·L^{-1} $NaHCO_3$ in deionized water) at a flow rate of 0.7 mL·min^{-1}. Sulfate was below the detection limit (detection limit: 100 μM) after 1 mo of incubation. The sediment slurry was stored at +4 °C for subsequent experiments.

I.3. Synthesized Model Compound [^{14}C]glucosyl-diphytanylglyceroldiether. The represented archaeal IPL, 1,2-di-*O*-phytanyl-*sn*-glycerol-3-glucosyl[U-^{14}C]glucose (GlcDGD), was synthesized by ARC Inc. from commercially available 1,2-di-*O*-phytanyl-*sn*-glycerol (Avanti Polar Lipids, Inc.), which is present in the "bacterial" *sn*-1,2 stereoconfiguration. Based on the assumption that enzymes are involved in the hydrolysis of the glycosidic bond, a potential effect of stereoselectivity on the activity of hydrolytic glycosidases is conceivable. However, in the case of this molecule, this selectivity is probably more sensitive to the stereochemistry of the sugar's alpha C-atom rather than to the stereogenic center of the glycerol C-atom in beta position.

I.4. Setup of Degradation Experiment. An experiment was conceived in which we monitored degradation of GlcDGD. Independent of the fate of the [^{14}C]glucosyl headgroup after hydrolysis from the glycerol backbone, the ^{14}C enters the aqueous or gas phase whereas the intact lipid is insoluble and remains in the sediment phase. Total degradation of GlcDGD then is obtained by combining the increase of radioactivity in the aqueous and gaseous phases.

Aliquots of 4 mL slurry were dispensed into a series of 5.9-mL Exetainer vials (Labco Limited) in the glove box. The headspace was replaced with N_2 and pressurized to atmospheric pressure. Then, 126 kBq (3.4 μCi) GlcDGD (equivalent to 45 ng/mL sediment slurry) was injected into the sediment slurry through the stopper in 30 μL dimethyl sulfoxide (≥99.8%, Rotipuran). After vortex mixing, vials of surface and subsurface sediment slurry were incubated in the dark at in situ temperature, 4 °C and 20 °C for 300 d, respectively. The sterilized slurry was stored at 20 °C. All incubations were carried out under N_2 headspace to ensure anaerobic conditions. The sampling frequency was high during the first half-month, i.e., after 1, 2, 7, and 14 d; thereafter, the sediment slurry was sampled every 2 mo. At each time point, samples were taken in triplicate for radioactivity measurements. At sampling, the headspace was flushed using synthetic air at 10 mL/min for 20 min. The gases were passed first through a 20-mL scintillation vial containing 10 mL Carbo-Sorb E (Perkin-Elmer) to trap [^{14}C]CO_2 and then through a heated CuO column (850 °C) in which [^{14}C]CH_4 was combusted into [^{14}C]CO_2; finally, the [^{14}C]CO_2 converted from [^{14}C]CH_4 was trapped in the second Carbo-Sorb E container. Before measurement, 10 mL Permafluor E^+ (Perkin-Elmer) was added to the scintillation vial. The radioactivity was quantified by liquid scintillation counting (LSC) (TR-2900; Canberra-Packard). Afterward, the sediment slurry was centrifuged at 2,000 rpm for 10 min (5810 R; Eppendorf). The aqueous phase was removed, and the sediment was rinsed three times with 2 mL Milli-Q water. The aqueous phases were combined with 10 mL LumaSafe Plus (Perkin-Elmer) for LSC measurement. After total radioactivity was measured in the aqueous phase, the combined aqueous phase was analyzed for ^{14}C-dissolved inorganic carbon (^{14}C-DIC) produced from degradation of IPLs. The aqueous phase was acidified to release carbon dioxide, which was trapped in scintillation vials with Permafluor E^+ (Perkin-Elmer), and the radioactivity was counted (6). After 300 d of incubation, no significant changes of radioactivity were detected (Fig. S1). This may be the result of either the rapid turnover of released [^{14}C]glucose or the relatively high limit of detection caused by the slight solubility (equivalent to 2% of initial radioactivity) of GlcDGD in water. Therefore, total degradation of GlcDGD was calculated by combining radioactivity of DIC, CH_4, and CO_2, leading to a minimum estimate.

II. SI Text

II.1. Determination of k′. The degradation rate of IPLs may be described by first-order kinetics (Eq. **S1**). For a short time interval Δt, k′ can be expressed using Eq. **S2** (7). Accordingly, k′ decreases exponentially with time (Eq. **S3**). In a previous study, Schouten

et al. (7) assumed that k′ is a constant during each sampling interval Δt, and therefore the k′ value was calculated for each sampling interval by Eq. **S2** from published data (8) for short time experiments with short sampling intervals. In the next step, these authors applied linear fitting between log k′ and log t (midpoint of each interval) according to Eq. **S3** to derive log a and b (intercept and slope). We refined the approach adopted by Schouten et al. (7) to account for the relatively long time intervals between sampling intervals, in which k′ cannot be considered constant. Using reverse fitting of experimental results, we derived refined values for a′ and b′ using Eq. **S4** (when $b \neq 1$), which results from integration of Eq. **S1** after substitution of k′ with Eq. **S3**. Values of a′ and b′ differ slightly from corresponding values derived by simple linear interpolation (Table S1).

The slope b′ (Eq. **S3**) for ester-bound IPLs (9), plotted as representative of typical bacterial IPLs (Fig. 1), is larger than b′ for GlcDGD, which suggests that k′ for ester-bound IPLs decreases at a faster rate compared with GlcDGD. However, large differences between the intercepts (log a′) of ester-bound IPLs and GlcDGD are consistent with the degradation rate constant of ester-bound IPLs being two to four orders of magnitude higher than those of GlcDGD. The slopes b′ for degradation of GlcDGD are similar for both sediments, but the higher a′ values of GlcDGD in active surface sediment relative to subsurface sediment result in k′ values an order of magnitude higher in the surface sediment.

II.2. Error Propagation for Degradation Kinetics of IPLs. To evaluate the effect of propagated errors introduced by the extrapolation of k′ to geologic time scales, we performed parallel modeling for each IPL group with a′ and b′ and their SEs generated from reverse fitting of experimental results (Eq. **S4**, when $b \neq 1$). We applied all possible combinations of a′ and b′ and their SEs for the subsequent modeling works, but only those cases resulting in the most extreme deviations of k′ are shown (Figs. S2–S4). The effects on k′ values of bacterial IPLs were comparatively small (Fig. S2*B*), but values for GlcDGD are associated with larger errors (Figs. S3*B* and S4*B*). Hence, the modeled bacterial IPL concentration is affected only slightly, whereas the modeled archaeal IPL concentration may differ by up to two orders of magnitude from values indicated in Fig. 2*C* (Figs. S3*D* and S4*D*). Consequently, in deeper sections of the 1-km model, when applying the faster Wadden Sea degradation kinetics for GlcDGD, in the extreme combinations of errors, the bacterial and IPL profiles might converge and become indistinguishable. However, even with maximum errors, most predictions using either the Wadden Sea or the Cascadia Margin kinetics are consistent with actual observations from samples in that they predict higher archaeal IPL concentrations.

II.3. Modeling Total Organic Carbon Degradation as Source of Carbon for Microbial Growth. Our simulation uses the fraction of organic carbon degraded over time in each given sediment interval as the source of carbon and energy for microbial growth. Degradation of total organic carbon (TOC) is derived according to the first-order kinetics (Eq. **S5**), where $[TOC_t]$ is the concentration of TOC at time t and k is the first-order rate constant (10). We assumed the sedimentation rate to be 10 cm·ky^{-1}; this corresponds to sediment ages of the sediment interval from 0.01 m to 1,000 m illustrated in our simulations from 10^2 y to 10^7 y. For a short time interval Δt, k can be presented using Eq. **S6** (10). If Δt is defined as sampling intervals and t as the midpoint of each interval, k is found to be exponentially decreasing with time (Eq. **S7**), where log a_{TOC} and $-b_{TOC}$ represent the intercept and the slope from a linear fit between log t and log k (10). Previous research documented a generally consistent decrease in the reactivity of TOC with time (b_{TOC}), but the initial reactivities (log a_{TOC}) are quite different and depend on the choice of apparent initial age ($t_{initial}$), which is an expression of the initial reactivity of TOC at the sediment–water interface (10). In our model, $t_{initial}$ is set to 10 ky (11). The sensitivity of the model to the choice of this parameter has been tested within a reasonable range of 1–100 ky. The relative differences of TOC and lipid turnover and concentration induced by this factor typically are substantially lower than a factor of two and thus are considered insignificant compared with potential errors induced by errors propagated through extrapolation of k′. The least-square fit between the reactivity of organic carbon (k) and time (t) is shown in Eq. **S8** (12), which is based on TOC concentration vs. depth under different conditions, such as sediment cores and laboratory experiments (10), and the water column (13). If Eq. **S5** is substituted with Eq. **S8**, the TOC degradation rate may be modeled. After integration of the degradation rate of TOC (integration of Eq. **S5** after substitution of k with Eq. **S8**), a depth profile of TOC concentration was obtained (Fig. 2*A*). If we set the average TOC content in surface sediments to 1% (11), the TOC depth profile in Fig. 2*A* is obtained, with the value of 0.2% at 1,000 m depth.

II.4. Modeling $IPL_{pro\text{-}TOC}$, IPL_{deg}, and Concentration of Archaeal and Bacterial IPLs. It has been demonstrated that carbon conversion efficiency of microbes is scaled with the free energy of their metabolism (14). The free-energy yield of the net metabolism in the deep biosphere cannot be constrained, but there is general consensus that microbially mediated biogeochemical reactions in sediments are close to thermodynamic equilibrium. We therefore chose the growth efficiency of one of the best-studied groups of anaerobic sedimentary microbes for our model, i.e., anaerobic methanotrophic archaea, which represent microbes living close to the biological energy quantum (15). For these, the carbon assimilation efficiency is 1% (16–18). We assume a sediment dry mass of 1 g·mL^{-1} sediment. For a cell diameter of 500 nm, the conversion factor cellular carbon/cellular IPL is 13 (11). To examine the effects of different degradation kinetics of archaeal and bacterial IPLs, we simply divide the flow of carbon from TOC to microbial lipids equally between Archaea and Bacteria, i.e., IPL production rates for Archaea and Bacteria are identical (Eq. **S9**). The effect of this factor on the degradation model also was examined for ratios of carbon flowing into Archaea vs. Bacteria of 10:90 and 90:10, respectively. The resulting trends of simulated concentrations of archaeal and bacterial IPLs generally are consistent with those from the 50:50 ratio (Fig. 2*C*) in that archaeal IPLs dominate, except for the 10:90 (Archaea:Bacteria) scenario, in which concentrations of both IPL types begin to converge. However, in this scenario archaeal IPLs in these deeper intervals were substantially lower than the actual observations. Degradation kinetics of ester-bound IPLs (9) and GlcDGD are described by Eq. **S4B** (when $b \neq 1$). By combining production and degradation of IPLs, IPL concentration can be modeled through a simple box-model (19) (Eq. **S10**). After integration of Eq. **S10**, depth profiles of archaeal and bacterial IPL concentrations are calculated by using the respective k′ values for these two IPL groups. Total IPL concentration is assumed to be 1,860 ng·mL^{-1} sediment at surface depth based on the intercept defined by the regression line (11); we assume that the IPL pool consists of equal fractions of archaeal and bacterial IPLs.

II.5. Half-Life of IPL, Biomass Turnover Times, and Percentage of Cellular IPL. We define the period required for IPLs at any given depth to decrease to 50% of the original concentration without considering potential input fluxes by in situ production as half-life ($t_{½}$) (Eq. **S11B**, when $b \neq 1$). Biomass turnover times are the time period required to accumulate the cellular concentration represented by the global regression line of directly counted microbial cells (20) with $IPL_{pro\text{-}TOC}$ [after conversion of IPL concentration into cell concentration using IPL cell^{-1} of 1.4 fg (11); Eq. **S12**]. If we assume that the cellular populations depicted by the regression line (20) consist of equal portions of Archaea and Bacteria (cf. ref. 11 for DNA-based evidence),

biomass turnover times are in the range of 1.6–73 ky from surface to 1,000 mbsf (Fig. 3*A*). The half-life of bacterial IPLs (0.017–53.4 ky) is much shorter than turnover of biomass above 100 mbsf, indicating that all bacterial IPL should be associated with cells. Below 100 m, the half-life of bacterial IPL is approaching cell turnover times, resulting in a small portion of bacterial IPL (less than 5%) as fossil (noncellular) components below 300 mbsf. Conversely, the half-life of archaeal IPL ranges from 20 to 312 ky from the top to the bottom of the 1-km sediment column, i.e., substantially longer than the biomass turnover times. Consequently, a substantial fraction of archaeal IPLs is noncellular (i.e., fossil). Percentage cellular (i.e., live) IPLs is derived from conversion of microbial cell concentrations derived from regression line (20) into IPL concentrations. This pool is defined to consist of 50% each of archaeal and bacterial IPLs; division of the archaeal or bacterial concentration through the respective IPL concentration derived from simulated TOC degradation yields the percentage of cellular IPLs. Values higher than 100%, derived for bacterial IPLs in some intervals, are no meaningful solution and therefore were depicted as 100%.

II.6. IPL Decay and Production in Relation to IPL Regression Line. The down-core profile of archaeal IPL concentration without in situ production was modeled by Eq. **S4** (Fig. 4*A*). IPL concentration at surface depth is set to 1,860 ng·mL^{-1} sediment, i.e., the intercept defined by the regression line (11). The production rate of archaeal IPL (IPL_{input}) is assumed to follow a power function (Eq. **S13**). If IPL_{input} is set to 1 ng·mL^{-1} sediment·y^{-1} at the 100-y-old surface of our model sediment column [according to stable isotope-probing results (21) that quantify archaeal lipid production rates in coastal sediment of similar age], the depth profile of archaeal IPL_{input} is described by Eq. **S14**. Based on the box-model (19), archaeal IPL_{input} was selected by adjusting slope (d′) to best match observed IPL concentration (Eq. **S15** and Fig. 4 *A* and *B*). For converting input rate of archaeal IPL to cell production rate, the amount of IPL cell^{-1} is 1.4 fg (11).

III. SI Equations

All mass units are in nanograms (10^{-9} g).

S1. First-Order Kinetics for IPL Degradation.

$$\frac{dIPL_t}{dt} = k' \times IPL_t, \qquad \textbf{[S1]}$$

where k′ is the rate constant and IPL_t is IPL concentration at time t.

S2. Expression of k′ During Short Time Interval Δt (Fig. 1*C*).

$$k' = \frac{1}{\Delta t} \times \ln \frac{IPL_t}{IPL_{(t+\Delta t)}}, \qquad \textbf{[S2]}$$

where k′ is a constant during short time sampling intervals Δt.

S3. Linear Fitting Between log k′ and log t (Fig. 1*C*).

$$\log k' = -b \times \log t + \log a, \qquad \textbf{[S3]}$$

where log a is intercept, b is slope.

S4. IPL Concentration at Time t. When b = 1,

$$IPL_t = IPL_0 \times \left(\frac{t}{t_0}\right)^{-a}. \qquad \textbf{[S4A]}$$

This equation is used to calculate the IPL concentration using a of 0.22 and b of 1 presented by Schouten et al. (7), when the modeled IPL concentration fits well with observed IPL concentration in the deep biosphere without any in situ production.

When b ≠ 1,

$$[IPL_t] = [IPL_0] \times e^{\frac{a'}{b'-1} \times \left(t^{1-b'} - t_0^{1-b'}\right)}. \qquad \textbf{[S4B]}$$

a′ and b′ are obtained by reverse fitting of experimental results (Fig. 1*C* and Figs. S2 *A* and *B*, S3 *A* and *B*, and S4 *A* and *B*).

S5. TOC Degradation (Fig. 2*A*).

$$\frac{dTOC_t}{dt} = k \times TOC_t, \qquad \textbf{[S5]}$$

where k is the degradation rate constant of TOC.

S6. Expression of k During Short Time Interval Δt.

$$k = \frac{1}{\Delta t} \times \ln \frac{TOC_t}{TOC_{(t+\Delta t)}}, \qquad \textbf{[S6]}$$

assuming that k is a constant during short time sampling interval Δt.

S7. Linear Fitting Between log k and log t.

$$k = a_{TOC} \times t^{-b_{TOC}} \text{ or } \log k = -b_{TOC} \times \log t + \log a_{TOC}, \qquad \textbf{[S7]}$$

where k is the degradation rate constant of TOC, log a_{TOC} is the intercept, and b_{TOC} is the slope.

S8. Least-Square Fit Between the Reactivity of Organic Carbon (k) and Time (t) (Fig. 2*A*).

$$k = -0.21 \times (t_{initial} + t)^{-0.985}, \qquad \textbf{[S8]}$$

where $t_{initial}$ is the apparent initial age (10,000 y, chosen according to ref. 11), which is an expression of the initial reactivity of TOC at the sediment–water interface (12).

S9. IPL Production Rate Estimated from TOC Decay (Fig. 2*B*).

$$IPL_{pro-TOC} = 0.21 \times (t + 10,000)^{-0.985} \times [TOC_t] \times 1\% \times \frac{1}{2} \times \frac{1}{13}, \qquad \textbf{[S9]}$$

where 10,000 is the apparent initial age (chosen according to ref. 11) and $[TOC_t]$ is the TOC concentration at time t, set to 1%. The carbon assimilation efficiency is assumed as 1% (16–18), $\frac{1}{2}$ is the carbon flow split ratio between Archaea and Bacteria, and $\frac{1}{13}$ is the ratio for cellular IPL vs. cellular carbon for a cell diameter of 500 nm [(11), calculated according to ref. 22].

S10. Box-Model for Modeling IPL Concentration from Input ($IPL_{pro-TOC}$) Flux (Eq. S9) and an Output (IPL_{deg}) Flux (Fig. 2*C*).

$$\frac{d[IPL_t]}{dt} = dIPL_{pro-TOC} - dIPL_{deg} = \left(0.21 \times (t + 10,000)^{-0.985} \times [TOC_t] \times 1\% \times \frac{1}{2} \times \frac{1}{13}\right) - (k' \times IPL_t) \qquad \textbf{[S10]}$$

Variables are the same as in Eq. **S9**; k′ is the degradation rate constant of IPL.

S11. Half-life of IPL. When b = 1,

$$t_{1/2} = t \times \left(2^{\frac{1}{a}} - 1\right). \qquad \textbf{[S11A]}$$

This equation is used to calculate the half-life of IPL (see the introduction) using the a of 0.22 and b of 1 presented by Schouten et al. (7).

When $b \neq 1$,

$$t_{1/2} = \left(t^{1-b'} + \ln 2 \times \frac{1-b'}{a'}\right)^{\frac{1}{1-b'}} - t. \quad \textbf{[S11B]}$$

a' and b' were obtained by reverse fitting of experimental results by Eq. **S4** (when $b \neq 1$) (Fig. 3*A*).

S12. Cellular Production Rate Converted from $IPL_{pro\text{-}TOC}$ (Fig. 3*A*).

$$Cell_{pro-TOC} = 0.21 \times (t + 10,000)^{-0.985} \times [TOC_t] \times 1\% \times \frac{1}{13} \times \frac{1}{1.4 \times 10^{-6}} \quad \textbf{[S12]}$$

where 10,000 is the apparent initial age for continental margin sediments (11), $[TOC_t]$ is the TOC concentration at time t, 1% is the assumed carbon assimilation efficiency of deep biosphere microbes (16–18), $\frac{1}{13}$ is the ratio for cellular IPL vs. cellular carbon, and the amount of IPL vs. cell is 1.4 fg for a cell diameter of 500 nm (11).

S13. The Input Rate of Archaeal IPL Production Rate (IPL_{input}) According to Power Function.

$$IPL_{input} = c' \times t^{-d'} \text{ or } \log IPL_{input} = -d' \times \log t + \log c' \quad \textbf{[S13]}$$

d' and $\log c'$ are the slope and intercept of $\log IPL_{input}$ and $\log t$.

S14. The Expression of Production Rate of Archaeal IPL (Fig. 4).

$$IPL_{input} = 1 \times \left(\frac{100}{t}\right)^{d'} \quad \textbf{[S14]}$$

If IPL_{input} rate is set to be 1 $ng \cdot mL^{-1}$ $sediment \cdot y^{-1}$ at surface sediment (21), Eq. **S13** will become $1 = c' \times 100^{-d'}$ (0.01 mbsf = 100 y) and therefore $c' = \left(\frac{1}{100}\right)^{-d'}$. After Eq. **S13** is substituted by c', the production rate of archaeal IPL may be expressed by Eq. **S14**. According to Eq. **S14**, the IPL_{input} rate is influenced only by d' (slope) and t in this equation.

S15. Box-Model to Determine IPL Concentration by Assuming It Is Related Only to an Input (IPL_{pro}) and an Output (IPL_{deg}) Flux (Fig. 4*A*).

$$\frac{d[IPL_t]}{dt} = dIPL_{pro} - dIPL_{deg} = \left(1 \times \left(\frac{100}{t}\right)^{d'}\right) - \left(k' \times IPL_t\right) \quad \textbf{[S15]}$$

IPL_{pro} follows the power function according to Eq. **S14**, whereas IPL_{deg} is according to Eq. **S1** with degradation rate constant k' of GlcDGD (Eq. **S4**) in different sediments (a' and b' values in Table S1).

1. De Beer D, Wenzhöfer F, Ferdelman TG, Boehme SE, Huettel M (2005) Transport and mineralization rates in North Sea sandy intertidal sediments, Sylt-Rømø Basin, Wadden Sea. *Limnol Oceanogr* 50(1):113–127.
2. Wilms R, et al. (2006) Specific bacterial, archaeal, and eukaryotic communities in tidal-flat sediments along a vertical profile of several meters. *Appl Environ Microbiol* 72(4): 2756–2764.
3. Seidel M, et al. (2012) Advection and diffusion determine vertical distribution of microbial communities in intertidal sediments as revealed by combined biogeochemical and molecular biological analysis. *Org Geochem* 52(0):114–129.
4. Expedition 311 Scientists (2006) Site U1326. *Proceedings of the Integrated Ocean Drilling Program*, eds Riedel M, Collett TS, Malone MJ; Expedition 311 Scientists (Integrated Ocean Drilling Program Management International, Washington, DC), Vol 311, 10.2204/iodp.proc.311.104.2006.
5. Heuer VB, Pohlman JW, Torres ME, Elvert M, Hinrichs K-U (2009) The stable carbon isotope biogeochemistry of acetate and other dissolved carbon species in deep subseafloor sediments at the northern Cascadia Margin. *Geochim Cosmochim Acta* 73 (11):3323–3336.
6. Treude T, Boetius A, Knittel K, Wallmann K, Jørgensen BB (2003) Anaerobic oxidation of methane above gas hydrates at Hydrate Ridge, NE Pacific Ocean. *Mar Ecol Prog Ser* 264:1–14.
7. Schouten S, Middelburg JJ, Hopmans EC, Sinninghe Damsté JS (2010) Fossilization and degradation of intact polar lipids in deep subsurface sediments: A theoretical approach. *Geochim Cosmochim Acta* 74(13):3806–3814.
8. Harvey HR, Fallon RD, Patton JS (1986) The effect of organic matter and oxygen on the degradation of bacterial membrane lipids in marine sediments. *Geochim Cosmochim Acta* 50(5):795–804.
9. Logemann AJ, et al. (2011) A laboratory experiment of intact polar lipid degradation in sandy sediments. *Biogeosciences* 8(9):2547–2560.
10. Middelburg JJ (1989) A simple rate model for organic matter decomposition in marine sediments. *Geochim Cosmochim Acta* 53(7):1577–1581.
11. Lipp JS, Morono Y, Inagaki F, Hinrichs K-U (2008) Significant contribution of Archaea to extant biomass in marine subsurface sediments. *Nature* 454(7207): 991–994.
12. Middelburg JJ, Vlug T, Van der Nat FJWA (1993) Organic matter mineralization in marine systems. *Global Planet Change* 8(1-2):47–58.
13. Suess E (1980) Particulate organic carbon flux in the oceans-surface productivity and oxygen utilization. *Nature* 288(5788):260–263.
14. Heijnen JJ, Van Dijken JP (1992) In search of a thermodynamic description of biomass yields for the chemotrophic growth of microorganisms. *Biotechnol Bioeng* 39(8): 833–858.
15. Hoehler TM, Alperin MJ, Albert DB, Martens CS (1994) Field and laboratory studies of methane oxidation in an anoxic marine sediment: Evidence for a methanogen-sulfate reducer consortium. *Global Biogeochem Cycles* 8(4):451–463.
16. Hinrichs K-U (2002) Microbial fixation of methane-carbon at 2.7 Ga: Was an anaerobic mechanism possible? *Geochem Geophys Geosyst* 3(7), 10.1029/2001GC000286.
17. Nauhaus K, Albrecht M, Elvert M, Boetius A, Widdel F (2007) In vitro cell growth of marine archaeal-bacterial consortia during anaerobic oxidation of methane with sulfate. *Environ Microbiol* 9(1):187–196.
18. Wegener G, Niemann H, Elvert M, Hinrichs K-U, Boetius A (2008) Assimilation of methane and inorganic carbon by microbial communities mediating the anaerobic oxidation of methane. *Environ Microbiol* 10(9):2287–2298.
19. Lipp JS, Hinrichs K-U (2009) Structural diversity and fate of intact polar lipids in marine sediments. *Geochim Cosmochim Acta* 73(22):6816–6833.
20. Parkes RJ, Cragg BA, Wellsbury P (2000) Recent studies on bacterial populations and processes in subseafloor sediments: A review. *Hydrogeol J* 8(1):11–28.
21. Wegener G, et al. (2012) Assessing sub-seafloor microbial activity by combined stable isotope probing with deuterated water and ^{13}C-bicarbonate. *Environ Microbiol* 14(6): 1517–1527.
22. Simon M, Azam F (1989) Protein content and protein synthesis rates of planktonic marine bacteria. *Mar Ecol Prog Ser* 51:201–213.

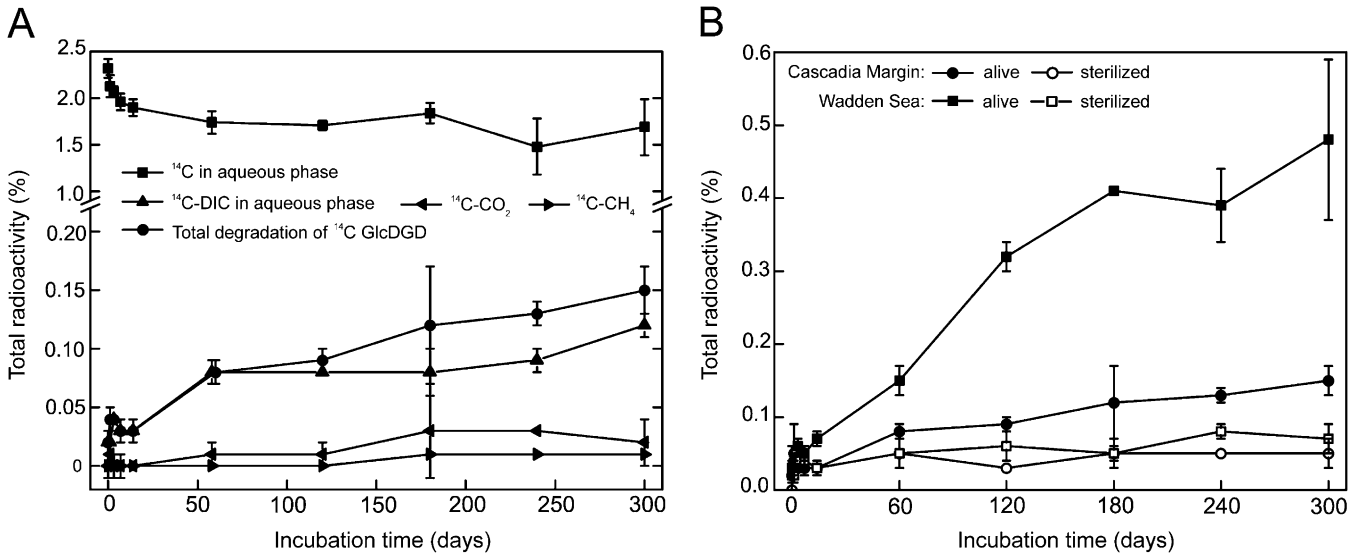

Fig. S1. (*A*) Degradation of [^{14}C]GlcDGD in Cascadia Margin sediment. Radioactivity was detected in gas phase ([^{14}C]CH_4, [^{14}C]CO_2) and aqueous phase (^{14}C-DIC). No significant change of radioactivity was detected in the aqueous phase during the 300-d incubation. Therefore, the reported total degradation of GlcDGD was calculated by combining [^{14}C]CH_4 and [^{14}C]CO_2 in gas phase and ^{14}C-DIC in aqueous phase. (*B*) Radioactivity release from [^{14}C]GlcDGD detected in four different experiments, detected as the sum of [^{14}C]CH_4, [^{14}C]CO_2, and ^{14}C-DIC. Results are presented as the average and SD of triplicate tubes.

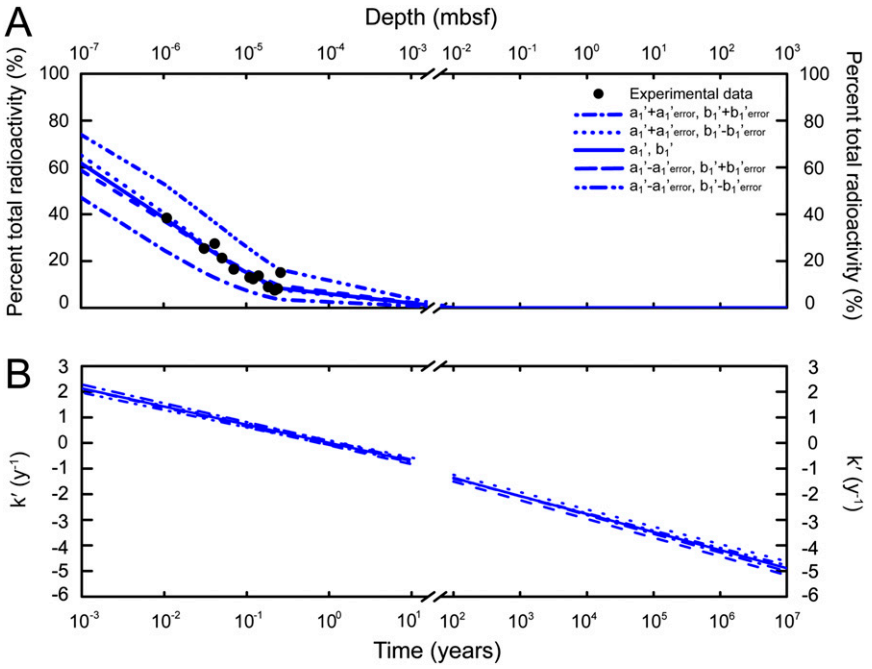

Fig. S2. Propagation of errors induced by extrapolation of k′ to geologic time scales for ester-bound IPLs. (*A*) Reverse fitting of experimental results of ester-bound IPLs (9). The different lines represent the extreme cases of the degradation rate of lipids influenced by SE of a′ and b′. (*B*) The effect of SE of a′ and b′ on k′ of ester-bound IPLs.

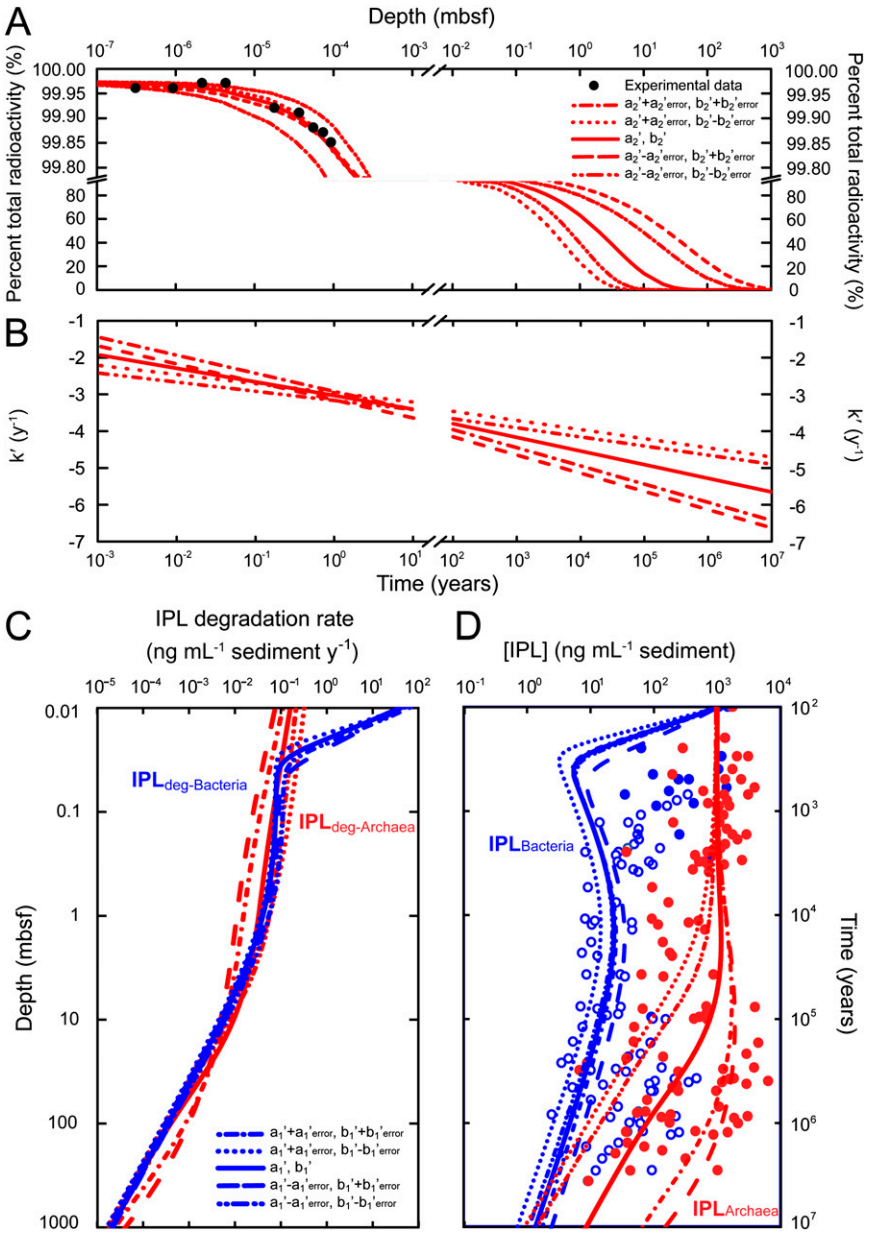

Fig. S3. Propagation of errors induced by extrapolation of k′ to geologic time scales for GlcDGD and its effects on concentration profiles of IPLs. (*A*) Reverse fitting of experimental results of GlcDGD in Cascadia Margin sediment. The different lines represent extreme cases of the degradation rate of lipids influenced by SE of a′ and b′. (*B*) The effect of SE of a′ and b′ on the degradation rate constant of GlcDGD. (*C*) The effect of SE of a′ and b′ on the degradation rate of archaeal IPLs and bacterial IPLs; the latter is identical to Fig. S4. (*D*) The effect of SE of a′ and b′ on the concentration of archaeal and bacterial IPLs.

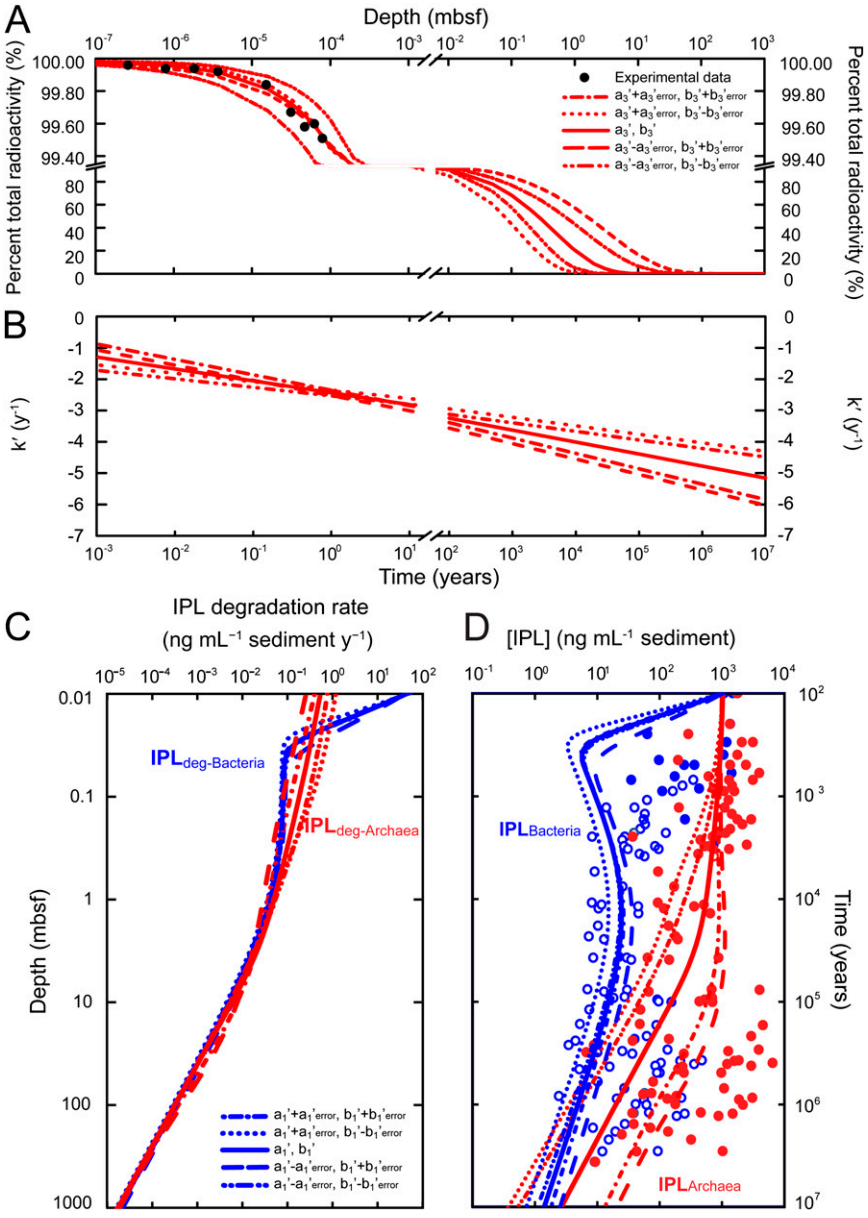

Fig. S4. Propagation of errors induced by extrapolation of k′ to geologic time scales for GlcDGD and its effects on concentration profiles of archaeal and bacterial IPLs. (*A*) Reverse fitting of experimental results of GlcDGD in Wadden Sea sediment. The different lines represent extreme cases of the degradation rate of lipids influenced by SE of a′ and b′. (*B*) The effect of SE of a′ and b′ on the degradation rate constant of GlcDGD. (*C*) The effect of SE of a′ and b′ on the degradation rate of archaeal IPLs and bacterial IPLs; the latter is identical to Fig. S3. (*D*) The effect of SE of a′ and b′ on concentration of archaeal IPLs and bacterial IPLs.

Table S1. Comparison of slopes (b and b′) and intercepts (log a and log a′) (Eqs. S2 and S4) derived from two different approaches to calculating degradation rate constant (k′)

Variable	a	b	a′	b′
$IPL_{ester\text{-}bound}$, WS (9)	1.428	0.776	1.101	0.704
GlcDGD, CM	0.0008	0.401	0.0009	0.371
GlcDGD, WS	0.004	0.356	0.0033	0.382

See *II. SI Text*, section II.1 for details. CM, Cascadia Margin; WS, Wadden Sea.